Journal of Alloys and Compounds 1080 (2026) 190321

Contents lists available at ScienceDirect

Journal of Alloys and Compounds

journal homepage: www.elsevier.com/locate/jalcom

Experimental determination of phase equilibria in the Co–Cr–Si ternary system

Kazushige Ioroi [a,*], Shunya Mochimaru [b], Xiao Xu [b], Ryosuke Kainuma [b], Toshihiro Omori [b]

[a] International Center for Young Scientists, National Institute for Materials Science (NIMS), Tsukuba 305-0047, Japan
[b] Department of Materials Science, Graduate School of Engineering, Tohoku University, 6-6-02 Aoba-yama, Sendai 980-8579, Japan

ARTICLE INFO

Keywords:
Cobalt-Chromium-Silicon
Phase diagram
Microstructure
Phase transformation
Metallic biomaterials

ABSTRACT

The phase equilibria of the Co–Cr–Si ternary system at 1000 and 1200 °C were comprehensively revisited using X-ray diffraction (XRD) analysis, microstructural observations, and quantitative compositional analysis by field-emission electron probe microanalyzer equipped with wavelength dispersive X-ray spectroscopy (FE-EPMA/WDS). Compared to previous work, the γ(Co)/ε(Co) phase boundary was newly established, and the solubility ranges of binary and ternary intermetallic compounds were successfully refined. Utilizing electron backscatter diffraction (EBSD) analysis, the compositional boundaries where the ε(Co) phase disappears were found to shift slightly toward the Co–Si-rich side with increasing temperature. Several binary silicide phases exhibited well-defined solubility ranges, and the β-Co_2Si phase was stabilized by Cr addition. The solubility range of the χ phase expanded toward the Cr–Si-rich side with increasing temperature, whereas that of the R phase contracted. The N phase was found to exist as a ternary compound adopting the Mn_5Si_3-type structure at 1200 °C, but it decomposed into β-Co_2Si and a eutectoid microstructure consisting of the (Co,Cr)Si and Cr_3Si phases at 1000 °C. Based on these results, isothermal sections of the Co–Cr–Si phase diagram at 1000 and 1200 °C were constructed.

1. Introduction

The global demand for biomaterials continues to grow as the elderly population increases worldwide. Metallic biomaterials account for approximately 70–80% of implanted medical devices and play a critical role in restoring the functionality of damaged hard tissues, thereby improving patients' quality of life. However, conventional metallic biomaterials, including stainless steels, Ti-based alloys, and Co–Cr alloys, still suffer from insufficient wear and corrosion resistances and limited biocompatibility. In particular, the large mismatch in Young's modulus between metallic implants and human bone often induces the stress-shielding effect, which accelerates bone resorption and reduces long-term implant stability [1,2].

Recently, Co–Cr–Al–Si (CCAS) alloys with the potential to overcome these limitations have been reported [3]. These alloys retain excellent wear and corrosion resistance while exhibiting an exceptionally low Young's modulus. Specifically, the Young's modulus of $<001>$-oriented single crystals is as low as 10–30 GPa, comparable to that of human cortical bone and considerably lower than that (190–240 GPa) of implant-grade stainless steels and conventional Co–Cr alloys [1,4]. Moreover, CCAS alloys show substantial superelasticity associated with a thermoelastic martensitic transformation from the B2 to the $L1_0$ structure, resulting in recoverable strains of up to 17%, nearly twice that of commercial Ti–Ni shape-memory alloys. These properties render CCAS alloys promising for the development of next-generation biomaterials.

Si plays a crucial role in the design of CCAS alloys. In the Co-rich part of the Co–Cr–Al ternary system, phase separation into A2 and B2 phases occurs during water quenching from the B2 single-phase region at high temperatures (over 1100 °C) [5], making it difficult to retain the ordered single-phase structure. However, an examination of the isothermal phase diagram at 1200 °C for the Co–Cr–(Al,Si) (Al:Si = 1:1) pseudo-ternary system revealed that Si addition considerably expands the B2 single-phase region compared with that in the Co–Cr–Al ternary system [6], facilitating martensite transformation in off-stoichiometric $Co_2Cr(Al,Si)$ alloys [3,7,8].

The CALPHAD (Calculation of Phase Diagrams) method predicts phase diagrams using thermodynamic parameters optimized based on phase-equilibrium data of binary and ternary systems, providing guidance for the design of multicomponent alloys. Recently, we conducted phase-equilibrium experiments at temperature exceeding 1500 °C [9,10] and determined the phase diagrams of the Co–Si [11], Co–Cr [12],

* Corresponding author.
E-mail address: IOROI.Kazushige@nims.go.jp (K. Ioroi).

https://doi.org/10.1016/j.jallcom.2026.190321
Received 17 June 2026; Received in revised form 27 July 2026; Accepted 6 August 2026
Available online 7 August 2026
0925-8388/© 2026 The Authors. Published by Elsevier B.V. This is an open access article under the CC BY license (http://creativecommons.org/licenses/by/4.0/).

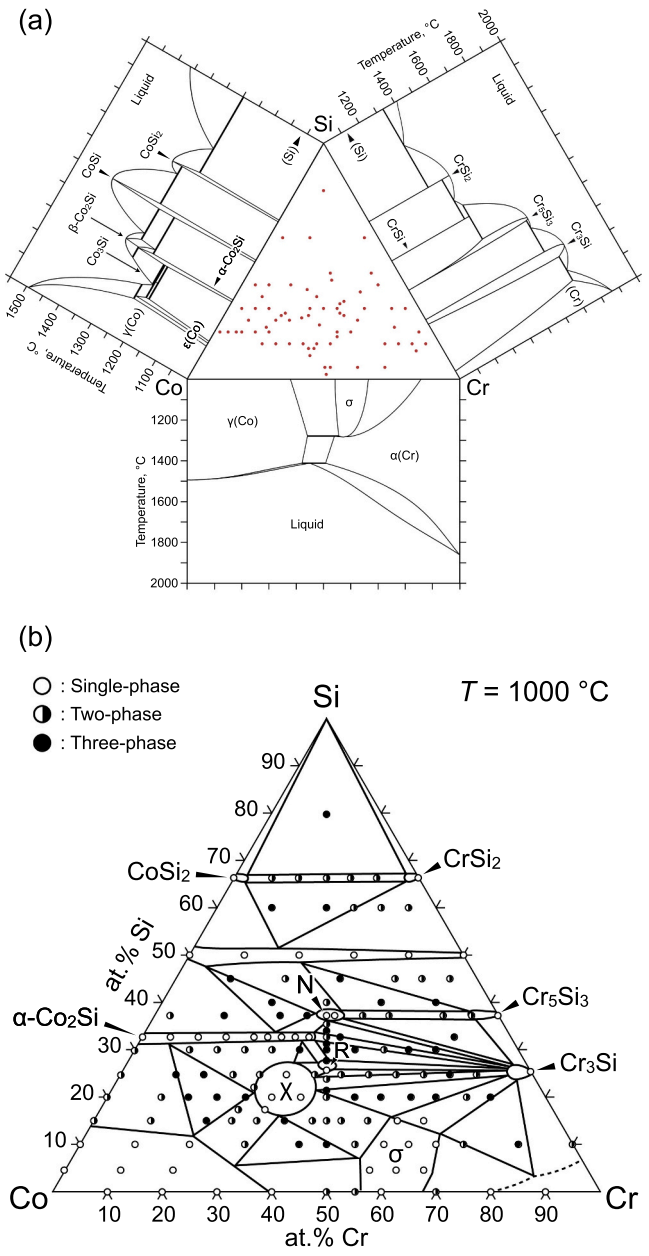


Fig. 1. (a) Nominal compositions (filled circles) of the Co–Cr–Si alloys examined in the present work and constituent binary phase diagrams: Co–Si [11], Co–Cr [12], and Cr–Si [13]. (b) Previously reported phase diagram of the Co–Cr–Si ternary system at 1000 °C [14].

and Cr–Si [10,13] binary systems, which are important binary subsystems of the Co–Cr–Si ternary system (Fig. 1(a)). A precise understanding of phase equilibria in the Co–Cr–Si ternary system is essential for optimizing CCAS alloy compositions and developing reliable thermodynamic databases for advanced biomaterials. However, the currently available phase diagram of the Co–Cr–Si ternary system exhibits limited accuracy in terms of individual phase boundaries, as it is based primarily on microstructural observations and X-ray diffraction (XRD) analyses [14], as illustrated in Fig. 1(b). To address this limitation, this study was aimed at experimentally revisiting the phase equilibria of the Co–Cr–Si ternary system.

2. Literature review

Several researchers have examined the phase equilibria of the Co–Cr–Si ternary system [14–16], enabling the construction of isothermal sections at various temperatures and the identification of multiple ternary intermediate phases. In 2010, Gupta reviewed experimental data regarding the phase equilibria in this system [17]. Details pertaining to stable solid phases and their crystal structures in the Co–Cr–Si system are presented in Table 1.

The earliest investigation into the Co–Cr–Si system at 1175 °C was conducted by Gupta et al. [15]. Alloys were prepared by arc melting electrolytic Co and Cr with high-purity Si under an Ar atmosphere, followed by annealing at 1175 °C for 72 h and water quenching. Using XRD and metallographic analyses, they constructed a partial isothermal section covering the region related to the σ phase extending from the Co–Cr binary system into the ternary system. They noted that the solubility limit of Si in the σ phase is approximately 17 at% and that the Cr_3Si phase extends substantially into the ternary region, reaching approximately 20 at% Co.

Borusevich and Gladyshevskiy [14] established isothermal sections at 800 and 1000 °C using XRD and metallographic analyses of annealed alloys. Specimens were prepared from electrolytic Cr (99.9%), Co (99.99%), and Si (99.96%) in corundum crucibles under an Ar atmosphere and subsequently heat-treated, although the annealing time was not reported. They determined the solubility ranges of the σ, Cr_3Si, Cr_5Si_3, and α-Co_2Si phases and identified two ternary compounds, i.e., the R (near the $Co_3Cr_3Si_2$ composition) and χ phases (near the $Co_5Cr_3Si_2$ composition). In addition, they proposed the existence of another ternary compound, termed the N phase (near $Co_{2.5}Cr_{2.5}Si_3$ composition), reported to be stable above 800 °C.

Kunitsin et al. [16] investigated the phase equilibria of the Co–Cr–Si ternary system at 1150 °C using electron probe microanalyzer (EPMA). Ingots were prepared from raw materials of Cr (99.9%), Co (99.99%), and Si (99.99%) using arc-melting. Both diffusion couples and equilibrated alloys were examined, and the specimens were heat-treated for 300 h. Experiments of $Co_{80}Si_{20}$/Cr and $Co_{20}Si_{80}$/Cr diffusion couples revealed the presence of solid-solution phases, intermetallic compounds, and an unidentified phase designated as the T phase in the Co–Cr–Si ternary system. EPMA measurements of equilibrated alloys confirmed that the T phase exhibits a solubility range of 24–29 at% Si and 3–7 at% Cr at 1150 °C. Additionally, they investigated the solubility ranges of other solid-solution, binary, and ternary compound phases and constructed an isothermal section of the phase diagram at 1150 °C.

3. Experimental procedures

Co–Cr–Si alloys were synthesized from high-purity Co (99.9%), Cr (99.99%), and Si (99.999%). The nominal compositions of the fabricated Co–Cr–Si alloys are indicated by the red filled circles in Fig. 1(a). Ingots were produced using a high-frequency induction melting furnace under an Ar atmosphere. These ingots were sliced into small specimens, and their surfaces were mechanically polished to remove oxide layers. Alloy compositions are reported in atomic percent (at%) unless otherwise noted.

Each specimen was encapsulated in a quartz glass tube filled with Ar gas. Subsequent heat treatments were conducted in electric resistance furnaces at 1000 and 1200 °C, followed by rapid quenching in ice water. The chemical compositions of the equilibrium phases were measured using a field-emission electron probe microanalyzer (FE-EPMA: JEOL JXA-8500F, Japan) equipped with wavelength-dispersive X-ray spectroscopes (WDS), operating at an accelerating voltage of 20 kV and a beam current of 10 nA. For each phase, concentrations were measured at

Table 1
Crystal structure information for three binary systems and one ternary system in the Co–Cr–Si system.

System	Phase	Pearson symbol	Space group	Strukturbericht designation	Structure	Proto-type	Lattice parameters, nm			Reference
							a	*b*	*c*	
Co–Si	γ(Co)	*cF4*	$Fm\bar{3}m$	A1	Cubic	Cu	0.3545	-	-	[18]
	ε(Co)	*hP2*	$P6_3/mmc$	A3	Hexagonal	Mg	0.2507	-	0.4070	[18]
	Co_3Si	-	-	-	-	-	-	-	-	-
	α-Co_2Si	*oP12*	*Pnma*	C23	Orthorhombic	Co_2Si	0.4918	0.7109	0.3738	[19,20]
	β-Co_2Si	*hP6*	$P6_3/mmc$	$B8_2$	Hexagonal	Ni_2In	0.3963	-	0.5024	[21]
	CoSi	*cP8*	$P2_13$	B20	Cubic	FeSi	0.4448	-	-	[22]
	$CoSi_2$	*cF12*	$Fm\bar{3}m$	C1	Cubic	CaF_2	0.5353	-	-	[23]
	(Si)	*cF8*	$Fd\bar{3}m$	A4	Diamond	C	0.5431	-	-	[24]
Co–Cr	γ(Co)	*cF4*	$Fm\bar{3}m$	A1	Cubic	Cu	0.3545	-	-	[18]
	ε(Co)	*hP2*	$P6_3/mmc$	A3	Hexagonal	Mg	0.2507	-	0.4070	[18]
	σ	*tP30*	$P4_2/mnm$	$D8_b$	Tetragonal	σCrFe	0.8758	-	0.4536	[17]
	α(Cr)	*cI2*	$Im\bar{3}m$	A2	Cubic	W	0.2910	-	-	[25]
Cr–Si	α(Cr)	*cI2*	$Im\bar{3}m$	A2	Cubic	W	0.2910	-	-	[25]
	Cr_3Si	*cP8*	$Pm\bar{3}n$	A15	Cubic	Cr_3Si	0.4558	-	-	[26,27]
	Cr_5Si_3	*tI38*	$I4/mcm$	$D8_m$	Tetragonal	W_5Si_3	0.9170	-	0.4636	[28]
	CrSi	*cP8*	$P2_13$	B20	Cubic	FeSi	0.4620	-	-	[29]
	$CrSi_2$	*hP9*	$P6_222$	C40	Hexagonal	$CrSi_2$	0.4428	-	0.6368	[30]
	(Si)	*cF8*	$Fd\bar{3}m$	A4	Diamond	C	0.5431	-	-	[24]
Co–Cr–Si	χ	*cI58*	$I\bar{4}3m$	A12	Cubic	αMn	0.8705	-	-	[31]
	R	*hR53*	$R\bar{3}$	$D8_a$	Rhombohedral	R(Co, Cr, Mo)	1.0587	-	1.8730	[17]
	N	-	-	-	-	-	-	-	-	-

10 distinct locations. Electron backscatter diffraction (EBSD) was used to identify the crystal orientation and structure. XRD analysis was performed using an X-ray diffractometer (Rigaku SmartLab, Japan) with Cu Kα radiation to determine the crystal structures of the Co–Cr–Si alloys.

4. Results and discussion

The equilibrium compositions of the Co–Cr–Si alloys heat-treated at 1000 and 1200 °C are summarized in Tables 2 and 3, respectively. Based on these results, isothermal phase diagrams of the Co–Cr–Si ternary system were constructed.

4.1. Phase equilibria on the Co–Cr-rich side

A narrow two-phase region exists between the γ(Co) and ε(Co) phases in both the Co–Si [11] and Co–Cr [12] binary systems. The ε(Co) phase remains stable up to the melting temperature in the Co–Si binary system [11], whereas it is stable only below 967 °C in the Co–Cr binary system [12]. In phase-equilibrium experiments of Co–Cr–Si ternary system, preparing samples with coexisting γ(Co) and ε(Co) phases is highly difficult due to its narrow two- or three-phase region, making it challenging to experimentally determine their phase equilibria. However, in this work, the composition range where the ε(Co) phase exists at 1000 °C and 1200 °C was successfully determined based on the difference in microstructural features between the originally stable ε(Co) phase and the transformed ε(Co) phase characterized by SEM observation and EBSD analysis. Figure 2 shows the microstructures of Co–Cr–Si alloys containing the γ(Co) and ε(Co) phases after equilibration at 1000 and 1200 °C. A distinct change in the microstructural features of the Co solid-solution phase is observed between the compositions Co–30Cr–15Si and Co–35Cr–15Si at 1000 °C (Fig. 2(b,c)) and between Co–25Cr–15Si and Co–30Cr–15Si at 1200 °C (Fig. 2(f,g)). In alloys with lower Cr contents, individual grains of the Co solid-solution phase exhibit a uniform contrast. In contrast, in alloys with higher Cr contents, the inclusions of Co solid-solution phase exhibit plate-like internal structures.

To further examine the microstructural characteristics, EBSD measurements were performed. Figure 3 presents the inverse pole figure (IPF) and phase maps of Co–Cr–Si alloys containing the γ(Co) and ε(Co) phases following heat treatment at 1000 and 1200 °C. Data points with confidence index (CI) values below 0.05 are excluded, and crystal orientation information is shown only for the γ(Co) and ε(Co) phases. The IPF map reveals difference in the microstructural features of the ε(Co) phase: The ε(Co) phase in the Co–25Cr–15Si alloy exhibits a single orientation within crystal grains (Fig. 3(c)). In contrast, the ε(Co) phase in the Co–30Cr–15Si alloy displays a more complex microstructure with different crystal orientations (Fig. 3(d)). Similar differences were observed between the microstructures of the Co–30Cr–15Si and Co–35Cr–15Si alloys heat-treated at 1000 °C (Fig. 3(a,b)). These microstructures were likely formed via transformation from the γ(Co) phase during cooling. Indeed, γ(Co) with a face-centered cubic structure has been reported to transform into a martensitic hexagonal close-

Table 2
Equilibrium compositions of the Co–Cr–Si ternary system at 1000 °C.

Nominal composition (at%)	Annealing time (h)	Equilibrium phase	Equilibrium composition (at%)					
		Phase 1 / Phase 2 / Phase 3	Phase 1		Phase 2		Phase 3	
			Cr	Si	Cr	Si	Cr	Si
Co–2Cr–20Si	72	ε(Co) / α-Co_2Si	2.6 ± 0.1	14.9 ± 0.2	0.7 ± 0.1	31.3 ± 0.1		
Co–5Cr–20Si	168	ε(Co) / α-Co_2Si	6.4 ± 0.1	15.4 ± 0.1	1.6 ± 0.1	31.8 ± 0.1		
Co–5Cr–40Si	168	β-Co_2Si / (Co,Cr)Si	8.3 ± 0.2	33.3 ± 0.2	0.5 ± 0.1	49.3 ± 0.1		
Co–8Cr–20Si	168	ε(Co) / α-Co_2Si	10.2 ± 0.1	15.2 ± 0.1	2.8 ± 0.1	31.3 ± 0.1		
Co–10Cr–20Si	168	ε(Co) / α-Co_2Si	12.7 ± 0.1	15.5 ± 0.1	3.8 ± 0.1	31.7 ± 0.1		
Co–10Cr–30Si	240	χ / α-Co_2Si	25.3 ± 0.4	21.6 ± 0.2	6.0 ± 0.1	32.1 ± 0.3		
Co–10Cr–35Si	336	β-Co_2Si / (Co,Cr)Si	11.1 ± 0.1	33.6 ± 0.1	1.2 ± 0.3	49.4 ± 0.2		
Co–10Cr–40Si	240	β-Co_2Si / (Co,Cr)Si	16.8 ± 1.0	33.3 ± 0.8	1.1 ± 0.1	49.2 ± 0.1		
Co–10Cr–80Si	120	$CoSi_2$ / $CrSi_2$ / (Si)	5.6 ± 1.0	65.8 ± 0.4	32.9 ± 0.1	66.7 ± 0.1	0.1 ± 0.1	99.8 ± 0.1
Co–15Cr–60Si	336	(Co,Cr)Si / $CoSi_2$ / $CrSi_2$	3.4 ± 0.2	50.1 ± 0.1	3.7 ± 0.1	64.6 ± 0.1	33.2 ± 0.2	65.9 ± 0.2
Co–18Cr–40Si	1200 °C 72 h → 168 h	β-Co_2Si / (Co,Cr)Si	24.7 ± 0.2	33.4 ± 0.4	2.2 ± 0.4	49.2 ± 0.4		
Co–20Cr–15Si	168	ε(Co) / χ	19.5 ± 0.1	13.9 ± 0.1	26.2 ± 0.2	19.1 ± 0.1		
Co–20Cr–20Si	1200 °C 1 h → 168 h	ε(Co) / χ / α-Co_2Si	16.3 ± 0.3	15.6 ± 0.1	23.5 ± 0.2	20.1 ± 0.2	5.5 ± 0.1	31.3 ± 0.1
Co–25Cr–15Si	168	ε(Co) / χ	22.8 ± 0.1	12.4 ± 0.2	29.1 ± 0.2	17.7 ± 0.2		
Co–25Cr–25Si	168	χ / β-Co_2Si	28.7 ± 0.1	23.2 ± 0.1	9.2 ± 0.1	32.3 ± 0.1		
Co–29Cr–26Si	1008	χ / R / β-Co_2Si	29.2 ± 0.1	23.5 ± 0.1	34.9 ± 0.1	24.4 ± 0.1	10.5 ± 0.4	32.1 ± 0.2
Co–30Cr–15Si	168	ε(Co) / χ	24.8 ± 0.2	11.3 ± 0.1	31.1 ± 0.1	16.7 ± 0.1		
Co–30Cr–45Si	1200 °C 120 h → 168 h	Cr_5Si_3 / (Co,Cr)Si	57.7 ± 0.4	37.1 ± 0.1	13.0 ± 0.4	49.3 ± 0.1		
Co–32Cr–42Si	336	Cr_5Si_3 / (Co,Cr)Si	55.5 ± 0.2	37.2 ± 0.3	5.3 ± 1.6	48.5 ± 0.6		
Co–35Cr–15Si	1200 °C 168 h → 168 h	γ(Co) / χ	29.8 ± 0.1	8.8 ± 0.4	35.2 ± 0.2	14.9 ± 0.1		
Co–35Cr–60Si	1200 °C 120 h → 168 h	(Co,Cr)Si / $CrSi_2$	37.6 ± 0.2	50.1 ± 0.3	33.5 ± 0.1	66.4 ± 0.1		
Co–37Cr–23Si	336	χ / R	33.3 ± 0.1	20.9 ± 0.1	38.3 ± 0.2	23.0 ± 0.1		
Co–38Cr–13Si	336	γ(Co) / σ / χ	31.0 ± 0.1	8.2 ± 0.1	45.1 ± 0.2	10.4 ± 0.1	36.6 ± 0.1	14.3 ± 0.1
Co–40Cr–10Si	1200 °C 72 h → 168 h	γ(Co) / σ	31.2 ± 0.1	8.1 ± 0.1	45.6 ± 0.1	10.3 ± 0.1		
Co–40Cr–30Si	1200 °C 72 h → 216 h	Cr_3Si / β-Co_2Si	71.6 ± 0.3	24.6 ± 0.2	23.7 ± 0.1	32.9 ± 0.1		
Co–42Cr–28Si	336	Cr_3Si / R	72.2 ± 1.5	24.5 ± 0.3	40.7 ± 0.2	27.7 ± 0.2		
Co–44Cr–27Si	336	Cr_3Si / R	72.1 ± 1.5	24.4 ± 0.3	42.1 ± 0.1	26.6 ± 0.1		
Co–45Cr–15Si	168	σ / χ	50.0 ± 0.2	13.5 ± 0.1	38.8 ± 0.1	16.9 ± 0.1		
Co–45Cr–37Si	1008	Cr_3Si / Cr_5Si_3 / (Co,Cr)Si	72.6 ± 1.9	25.2 ± 0.7	56.1 ± 0.2	36.8 ± 0.1	5.7 ± 1.8	48.2 ± 0.6
Co–45Cr–45Si	1200 °C 120 h→ 168 h	Cr_5Si_3 / (Co,Cr)Si	59.4 ± 0.2	37.7 ± 0.1	35.2 ± 0.2	49.6 ± 0.1		
Co–46Cr–18Si	336	σ / χ / R	51.7 ± 0.1	14.5 ± 0.1	39.3 ± 0.2	17.8 ± 0.2	43.5 ± 0.1	20.8 ± 0.2
Co–48Cr–5Si	168	γ(Co) / σ	36.1 ± 0.2	3.1 ± 0.1	51.3 ± 0.1	4.5 ± 0.1		
Co–50Cr–25Si	336	Cr_3Si / R	71.8 ± 0.9	23.9 ± 0.1	43.6 ± 0.2	24.6 ± 0.2		
Co–65Cr–15Si	168	σ / Cr_3Si	62.8 ± 0.4	13.2 ± 0.3	72.9 ± 0.7	22.8 ± 0.5		
Co–65Cr–22Si	1200 °C 72 h → 216 h	σ / R / Cr_3Si	56.3 ± 0.1	15.7 ± 0.1	45.5 ± 0.1	22.0 ± 0.1	70.4 ± 0.8	23.8 ± 0.1
Co–65Cr–30Si	1200 °C 72 h → 168 h	Cr_3Si / Cr_5Si_3	73.2 ± 0.1	24.7 ± 0.1	55.1 ± 0.2	36.9 ± 0.1		
Co–70Cr–15Si	1200 °C 168 h → 168 h	σ / Cr_3Si	67.7 ± 0.3	11.5 ± 0.3	74.2 ± 0.1	20.2 ± 0.1		
Co–78Cr–12Si	1200 °C 168 h → 168 h	α(Cr) / σ / Cr_3Si	89.1 ± 0.2	4.1 ± 0.1	69.6 ± 0.1	10.3 ± 0.2	76.4 ± 0.2	17.7 ± 0.1
Co–80Cr–15Si	1200 °C 168 h → 168 h	α(Cr) / Cr_3Si	89.8 ± 0.1	4.0 ± 0.1	76.2 ± 0.2	19.5 ± 0.1		

packed phase during water quenching in Co–8Si binary alloys [32]. According to the phase maps (Fig. 3(e–h)), all Co–Cr–Si alloys primarily consist of the ε(Co) and χ phases. The γ(Co) phase is also detected in the Co–35Cr–15Si alloy heat-treated at 1000 °C and Co–30Cr–15Si alloy heat-treated at 1200 °C, as shown in Figs. 3(f,h), suggesting partial retention of the γ(Co) phase during water quenching. This indicates that the ε(Co) phase extends toward the Cr-rich side. It disappears across the compositional ranges from 63.9Co–24.8Cr–11.3Si (at%) to 61.4Co–29.8Cr–8.8Si (at%) at 1000 °C and from 60.7Co–25.2Cr–14.1Si (at%) to 59.7Co–28.3Cr–12.0Si (at%) at 1200 °C, representing phase boundaries of the ε(Co) phase in the alloys discussed above.

Figure 4 shows typical microstructures of Co–Cr–Si alloys with low Si contents after heat treatment at 1000 and 1200 °C for various durations. The size of each phase was sufficiently large to enable quantitative analysis by FE-EPMA/WDS. Although several additional regions with different contrasts are observed in these microstructures, especially in Figs. 4(b), 4(c), 4(d), and 4(f), these variations arise from channeling contrast for the labeled phases due to differences in crystallographic orientation rather than the presence of additional phases. Figure 5 presents the phase diagrams focused on the Co–Cr-rich region. As shown in Fig. 4(a), the Co–20Cr–20Si alloy heat-treated at 1200 °C for 24 h exhibits an inhomogeneous microstructure in addition to the ε(Co) and χ phases. This microstructure likely consists of primary crystals along with a fine eutectic microstructure, suggesting that it originates from a liquid phase stable at 1200 °C that transforms into solid phases during water quenching (inset of Fig. 4(a)). In this study, the composition of the liquid phase was determined by averaging 10 compositional measurements. However, accurately determining the equilibrium composition remains difficult owing to the heterogeneous nature of the microstructure; thus, the compositions reported herein may exhibit a certain degree of scatter.

The FE-EPMA/WDS measurements reveal the presence and compositional ranges of the ternary χ and R phases. As indicated in Table 2 and Fig. 5(a), the χ phase exhibits a solubility range of 23.5–39.3 at% Cr and 14.3–23.5 at% Si at 1000 °C, which is broader than that reported by Borusevich and Gladyshevskiy [14]. The R phase displays a solubility range of 34.9–45.5 at% Cr and 20.8–27.7 at% Si at 1000 °C, consistent with prior results [14]. Compared with the phase diagram at 1000 °C, the solubility range of the χ phase at 1200 °C expands toward the Cr–Si-rich side, whereas that of the R phase shows a tendency to shrink, as shown in Tables 2 and 3, and Fig. 5(b).

The present work also reveals that Si dissolves significantly in the σ phase, expanding its Cr solubility limits to a wide range of

Table 3
Equilibrium compositions of the Co–Cr–Si ternary system at 1200 °C.

Nominal composition (at%)	Annealing time (h)	Equilibrium phase	Equilibrium composition (at%)					
		Phase 1 / Phase 2 / Phase 3	Phase 1		Phase 2		Phase 3	
			Cr	Si	Cr	Si	Cr	Si
Co–2Cr–20Si	72	ε(Co) / Co_3Si	2.3 ± 0.1	17.6 ± 0.1	1.7 ± 0.1	24.1 ± 0.1		
Co–5Cr–20Si	72	ε(Co) / Co_3Si	5.6 ± 0.1	17.4 ± 0.1	4.5 ± 0.1	24.5 ± 0.2		
Co–5Cr–30Si	120	Co_3Si / α-Co_2Si	9.4 ± 0.6	24.4 ± 0.5	3.7 ± 0.1	31.8 ± 0.1		
Co–5Cr–40Si	96	β-Co_2Si / (Co,Cr)Si	8.3 ± 0.3	34.4 ± 0.7	0.6 ± 0.1	49.0 ± 0.1		
Co–5Cr–60Si	96	(Co,Cr)Si / $CoSi_2$	9.6 ± 0.3	50.6 ± 0.1	3.1 ± 0.1	64.7 ± 0.1		
Co–8Cr–20Si	72	ε(Co) / Co_3Si	8.8 ± 0.1	16.8 ± 0.2	7.3 ± 0.1	23.9 ± 0.2		
Co–10Cr–20Si	72	ε(Co) / Co_3Si	11.0 ± 0.2	17.2 ± 0.2	9.2 ± 0.1	24.3 ± 0.2		
Co–10Cr–30Si	72	Co_3Si / α-Co_2Si	15.3 ± 0.1	25.4 ± 0.3	7.6 ± 0.1	32.0 ± 0.4		
Co–10Cr–35Si	72	β-Co_2Si / (Co,Cr)Si	10.8 ± 0.7	33.7 ± 0.3	1.2 ± 0.1	48.5 ± 0.2		
Co–10Cr–40Si	72	β-Co_2Si / (Co,Cr)Si	16.3 ± 0.3	33.5 ± 0.2	1.4 ± 0.1	49.0 ± 0.1		
Co–10Cr–80Si	72	$CoSi_2$ / $CrSi_2$ / (Si)	1.9 ± 0.2	66.3 ± 0.2	33.0 ± 0.2	66.6 ± 0.1	0.1 ± 0.1	99.8 ± 0.1
Co–15Cr–20Si	0.5	ε(Co) / Co_3Si	16.3 ± 0.1	16.4 ± 0.1	14.1 ± 0.1	23.6 ± 0.1		
Co–15Cr–30Si	72	Co_3Si / β-Co_2Si	19.4 ± 0.1	25.6 ± 0.1	13.7 ± 0.3	31.6 ± 0.2		
Co–15Cr–60Si	96	(Co,Cr)Si / $CoSi_2$ / $CrSi_2$	12.4 ± 0.2	50.4 ± 0.8	4.2 ± 0.3	64.3 ± 0.2	32.6 ± 0.5	66.1 ± 0.2
Co–18Cr–40Si	96	β-Co_2Si / N / (Co,Cr)Si	24.8 ± 0.3	33.9 ± 0.9	30.5 ± 0.3	37.7 ± 0.6	3.3 ± 0.1	49.0 ± 0.3
Co–20Cr–20Si	24	ε(Co) / χ / Liquid	21.3 ± 0.2	16.3 ± 0.1	25.6 ± 0.2	20.3 ± 0.1	21.0 ± 3.3	21.1 ± 1.5
Co–21Cr–27Si	168	χ / Co_3Si / β-Co_2Si	29.2 ± 0.1	23.8 ± 0.1	22.1 ± 0.3	25.5 ± 0.1	16.0 ± 0.3	31.4 ± 0.2
Co–22Cr–28Si	168	χ / β-Co_2Si	28.9 ± 0.1	23.8 ± 0.1	15.8 ± 0.1	31.3 ± 0.1		
Co–25Cr–15Si	168	ε(Co) / χ	25.2 ± 0.2	14.1 ± 0.2	30.1 ± 0.1	18.3 ± 0.1		
Co–25Cr–25Si	96	χ / Co_3Si	29.4 ± 0.1	23.8 ± 0.1	22.1 ± 0.1	25.6 ± 0.1		
Co–30Cr–15Si	168	γ(Co) / χ	28.3 ± 0.1	12.0 ± 0.1	33.1 ± 0.1	16.7 ± 0.1		
Co–30Cr–30Si	72	R / β-Co_2Si	39.0 ± 0.3	26.3 ± 0.3	23.1 ± 0.1	32.6 ± 0.2		
Co–30Cr–45Si	96	Cr_5Si_3 / (Co,Cr)Si	55.8 ± 0.1	37.4 ± 0.1	13.4 ± 0.1	49.3 ± 0.2		
Co–31Cr–27Si	168	χ / R / β-Co_2Si	32.7 ± 0.2	24.7 ± 0.1	37.0 ± 0.2	25.4 ± 0.1	20.2 ± 0.1	31.8 ± 0.1
Co–32Cr–42Si	168	Cr_5Si_3 / N / (Co,Cr)Si	51.7 ± 0.1	36.9 ± 0.1	38.3 ± 0.2	37.3 ± 0.2	5.9 ± 0.5	48.8 ± 0.2
Co–35Cr–15Si	72	γ(Co) / χ	31.2 ± 0.1	10.2 ± 0.1	36.2 ± 0.1	15.3 ± 0.1		
Co–35Cr–60Si	96	(Co,Cr)Si / $CrSi_2$	37.9 ± 0.2	49.8 ± 0.2	33.8 ± 0.1	65.8 ± 0.1		
Co–37Cr–23Si	168	χ / R	36.4 ± 0.1	22.2 ± 0.1	40.3 ± 0.1	23.6 ± 0.1		
Co–40Cr–10Si	336	γ(Co) / σ	34.3 ± 0.1	8.9 ± 0.1	45.5 ± 0.2	10.3 ± 0.1		
Co–40Cr–13Si	1400 °C 24 h → 72 h	γ(Co) / σ / χ	32.6 ± 0.1	10.8 ± 0.1	43.0 ± 0.2	12.6 ± 0.1	37.0 ± 0.1	15.8 ± 0.1
Co–40Cr–30Si	120	Cr_3Si / β-Co_2Si	70.0 ± 0.6	24.7 ± 0.6	26.7 ± 0.3	33.1 ± 0.5		
Co–41Cr–33Si	168	Cr_3Si / β-Co_2Si / N	71.5 ± 1.0	25.0 ± 0.4	29.6 ± 0.5	33.4 ± 0.3	37.9 ± 0.4	37.5 ± 0.8
Co–42Cr–28Si	168	Cr_3Si / R / β-Co_2Si	70.6 ± 0.2	24.1 ± 0.2	41.0 ± 0.3	27.1 ± 0.2	26.8 ± 0.5	32.7 ± 0.3
Co–44Cr–27Si	720	Cr_3Si / R	70.5 ± 0.1	24.4 ± 0.1	41.2 ± 0.2	26.9 ± 0.1		
Co–45Cr–15Si	1400 °C 48 h → 168 h	σ / χ	47.0 ± 0.2	14.2 ± 0.2	39.1 ± 0.3	17.3 ± 0.1		
Co–45Cr–20Si	168	σ / χ / R	51.6 ± 0.1	17.3 ± 0.1	40.9 ± 0.1	20.0 ± 0.1	43.5 ± 0.2	22.3 ± 0.1
Co–45Cr–45Si	168	Cr_5Si_3 / (Co,Cr)Si	59.1 ± 0.1	38.0 ± 0.2	35.2 ± 0.1	49.6 ± 0.1		
Co–46Cr–18Si	168	σ / χ	50.7 ± 0.2	16.3 ± 0.1	40.7 ± 0.2	19.2 ± 0.1		
Co–48Cr–5Si	72	γ(Co) / σ	39.2 ± 0.2	3.6 ± 0.1	51.3 ± 0.1	4.5 ± 0.1		
Co–50Cr–25Si	72	Cr_3Si / R	70.4 ± 0.5	23.6 ± 0.4	43.3 ± 0.5	24.4 ± 0.3		
Co–50Cr–40Si	1300 °C 72 h → 72 h	Cr_5Si_3 / (Co,Cr)Si	57.1 ± 0.2	37.5 ± 0.2	17.3 ± 0.2	49.5 ± 0.1		
Co–60Cr–30Si	168	Cr_3Si / Cr_5Si_3 / N	72.0 ± 0.2	24.8 ± 0.1	51.4 ± 0.2	36.5 ± 0.1	38.5 ± 0.2	37.3 ± 0.2
Co–65Cr–15Si	1400 °C 48 h → 168 h	σ / Cr_3Si	64.2 ± 0.1	13.6 ± 0.1	73.0 ± 0.2	21.6 ± 0.2		
Co–65Cr–22Si	240	σ / R / Cr_3Si	53.6 ± 0.2	18.4 ± 0.1	44.6 ± 0.3	22.8 ± 0.2	69.9 ± 0.1	23.6 ± 0.2
Co–65Cr–30Si	168	Cr_3Si / Cr_5Si_3	73.0 ± 0.2	24.7 ± 0.2	54.7 ± 0.2	36.6 ± 0.1		
Co–70Cr–5Si	168	α(Cr) / σ	78.7 ± 0.1	3.1 ± 0.1	67.6 ± 0.2	5.5 ± 0.1		
Co–70Cr–15Si	168	σ / Cr_3Si	68.3 ± 0.2	12.0 ± 0.1	74.4 ± 0.1	20.5 ± 0.3		
Co–78Cr–12Si	336	α(Cr) / σ / Cr_3Si	83.5 ± 0.1	6.5 ± 0.1	70.5 ± 0.2	11.4 ± 0.2	75.2 ± 0.2	19.0 ± 0.2
Co–80Cr–15Si	72	α(Cr) / Cr_3Si	87.4 ± 0.2	5.8 ± 0.1	76.2 ± 0.3	19.9 ± 0.1		

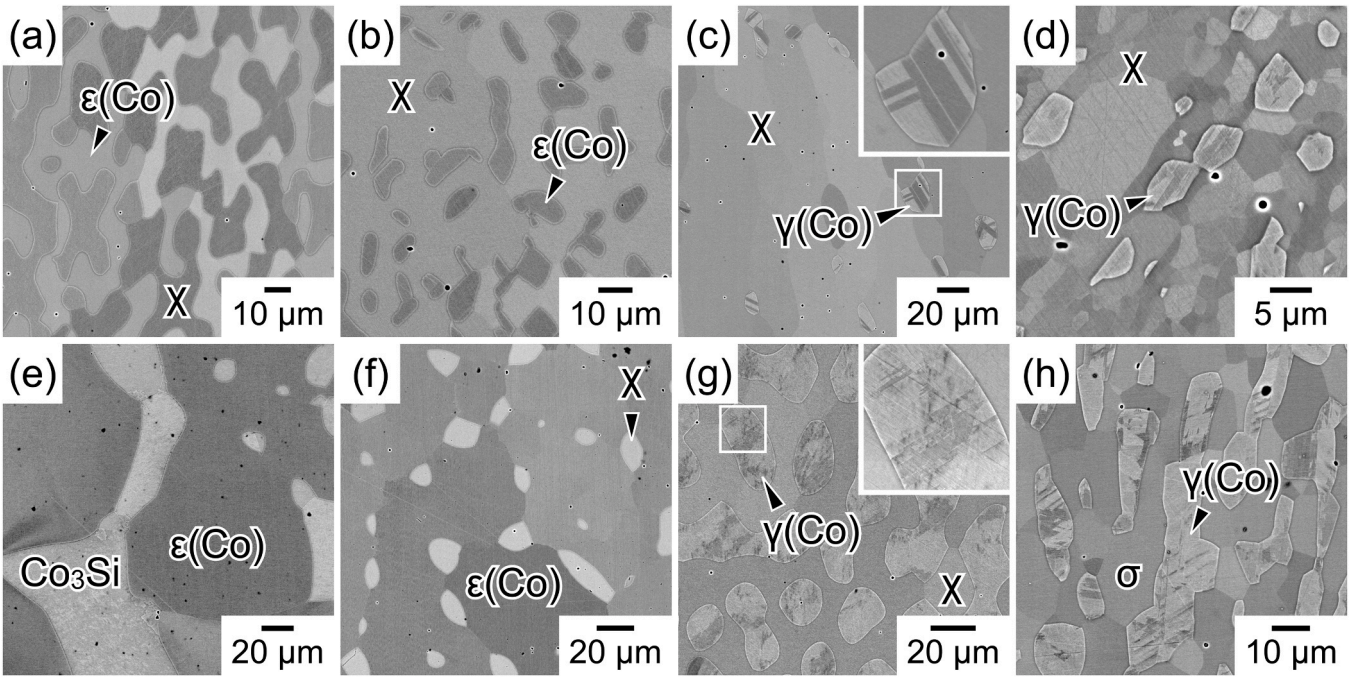


Fig. 2. Back-scattered electron (BSE) images of microstructures in the (a) Co–25Cr–15Si, (b) Co–30Cr–15Si, (c) Co–35Cr–15Si, and (d) Co–38Cr–13Si alloys heat-treated at 1000 °C, and (e) Co–10Cr–20Si, (f) Co–25Cr–15Si, (g) Co–30Cr–15Si, and (h) Co–40Cr–10Si alloys heat-treated at 1200 °C. The insets in (c) and (g) show magnified views of the γ-(Co) phase.

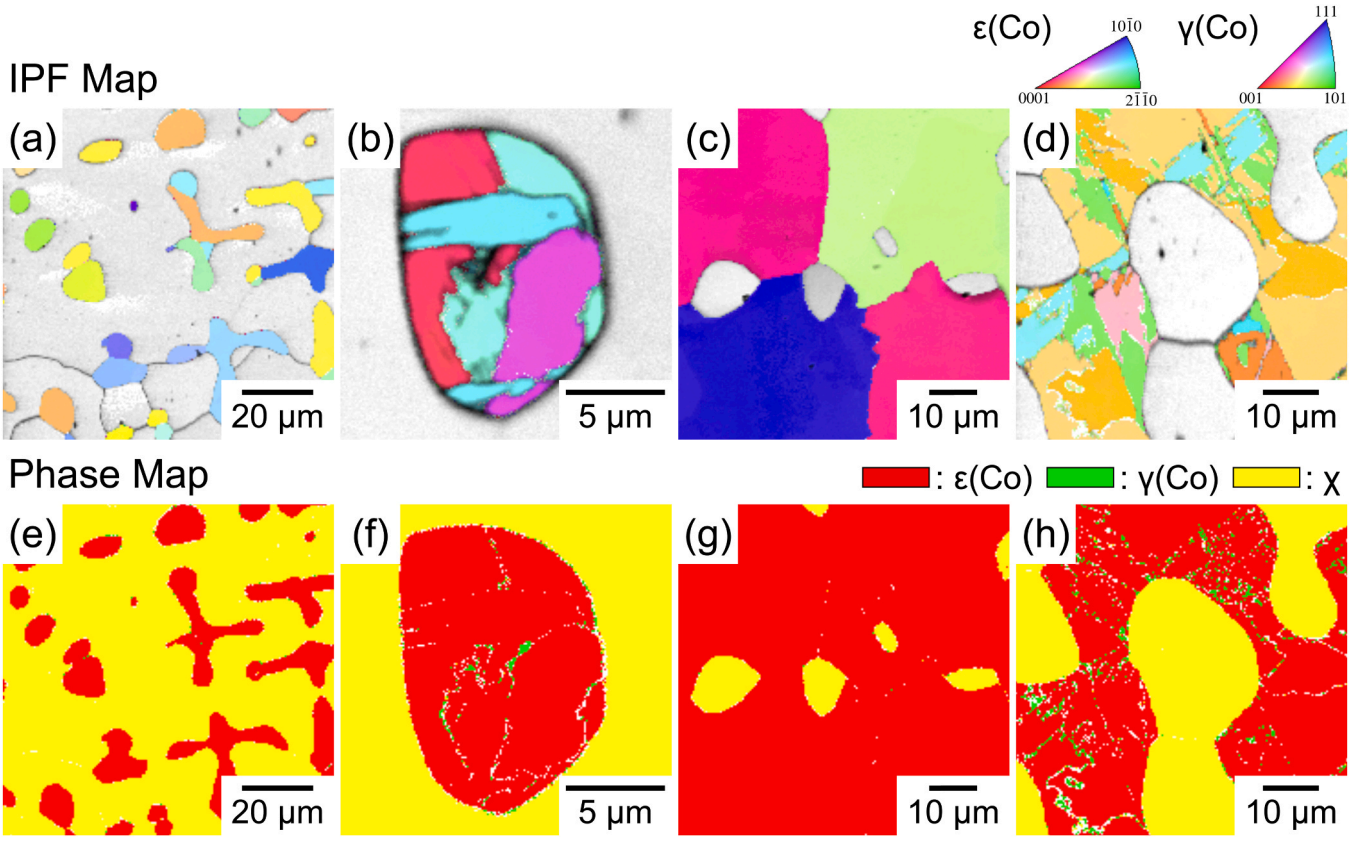


Fig. 3. (a–d) Inverse pole figure (IPF) and (e–h) phase maps of Co–Cr–Si alloys containing γ(Co) and ε(Co) phases: (a, e) Co–30Cr–15Si heat-treated at 1000 °C for 168 h; (b, f) Co–35Cr–15Si heat-treated at 1000 °C for 168 h; (c, g) Co–25Cr–15Si heat-treated at 1200 °C for 168 h; and (d, h) Co–30Cr–15Si heat-treated at 1200 °C for 168 h. Data points with a confidence index below 0.05 are excluded, and crystal orientation information is shown only for the γ(Co) and ε(Co) phases (IPF maps).

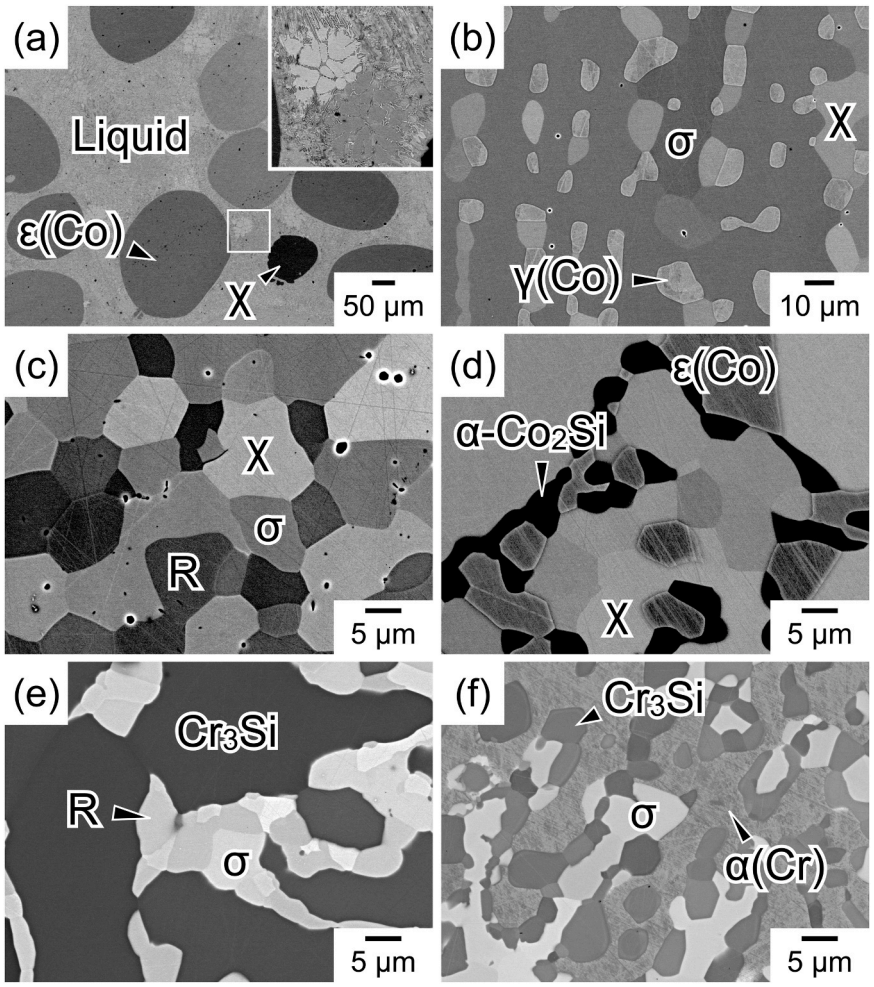


Fig. 4. BSE images of three-phase microstructures in (a) Co–20Cr–20Si alloy heat-treated at 1200 °C for 24 h (the inset shows a magnified view of the microstructure derived from the liquid phase); (b) Co–40Cr–13Si alloy heat-treated at 1200 °C for 72 h; (c) Co–45Cr–20Si alloy heat-treated at 1200 °C for 168 h; (d) Co–20Cr–20Si alloy heat-treated at 1200 °C for 1 h; (e) Co–65Cr–22Si alloy heat-treated at 1000 °C for 216 h after homogenization at 1200 °C for 72 h; and (f) Co–78Cr–12Si alloy heat-treated at 1200 °C for 168 h.

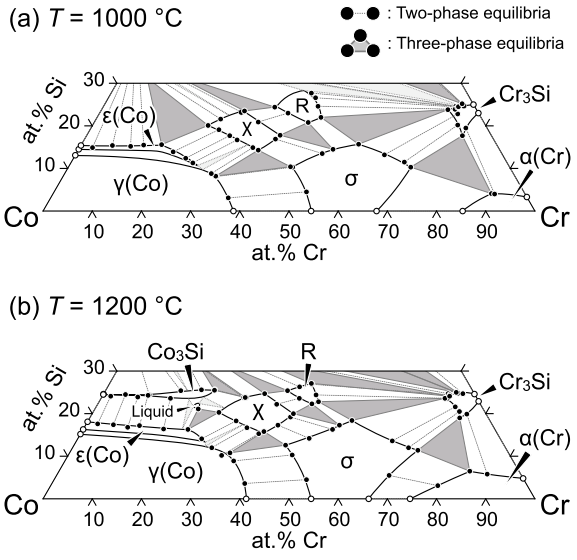


Fig. 5. Phase diagram enlarged for the Co–Cr-rich portion at (a) 1000 °C and (b) 1200 °C.

approximately 45–70 at% Cr as the Si content increases (Figs. 5(a) and 5(b)). The σ phase can contain up to 15.7 at% Si at 1000 °C, which further increases to 18.4 at% Si at 1200 °C. These findings indicate that Si strongly stabilizes the σ phase at these elevated temperatures.

4.2. Phase equilibria of binary silicide compounds

Figure 6 shows the microstructures of Co–Cr–Si alloys with the α- and β-Co_2Si phases after heat treatment at 1000 and 1200 °C. As indicated in Table 2, the equilibrium Cr content in the α- and β-Co_2Si phases at 1000 °C increases with increasing Si content in the Co–10Cr–*x*Si alloys. Moreover, the microstructural characteristics change markedly with increasing Cr content in the α- and β-Co_2Si phases, as shown in Fig. 6(a)–(d). The phase with lower Cr content (labeled as α-Co_2Si) exhibits a single-phase microstructure in the alloys shown in Figs. 6(a) and 6(b). In contrast, fine two-phase microstructures are observed in regions labeled as β-Co_2Si in Figs. 6(c) and 6(d). For these regions, the chemical compositions of the β-Co_2Si two-phase region were measured at randomly selected points and averaged. A fine two-phase microstructure is also observed in the Co–5Cr–40Si and Co–10Cr–35Si alloys heat-treated at 1200 °C, as shown in Figs. 6(g) and 6(h). These microstructures are similar to those transformed from the β-Co_2Si phase in our previous work on the Co–Si phase diagram [9], where they were considered to consist of the primary precipitated α-Co_2Si phase and fine microstructure of the α-Co_2Si and CoSi phases. In the Co–Si binary system, α-Co_2Si

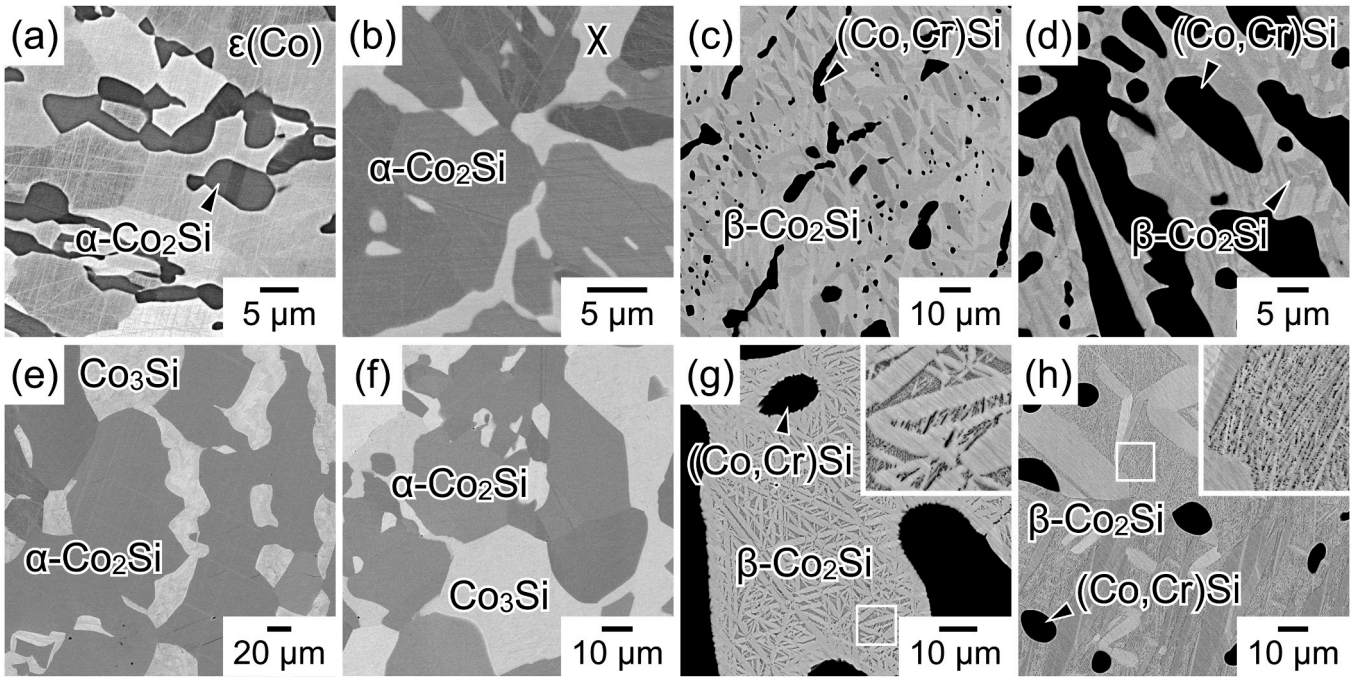


Fig. 6. BSE images of microstructures containing α- and β-Co_2Si phases: (a) Co–10Cr–20Si, (b) Co–10Cr–30Si, (c) Co–10Cr–35Si, and (d) Co–10Cr–40Si alloys heat-treated at 1000 °C, and (e) Co–5Cr–30Si, (f) Co–10Cr–30Si, (g) Co–5Cr–40Si, and (h) Co–10Cr–35Si heat-treated at 1200 °C. The insets in (g) and (h) show magnified views of the β-Co_2Si phase.

and β-Co_2Si phases are low-temperature and high-temperature phases, respectively. The β-Co_2Si phase cannot be retained by water quenching as it is stable only at temperatures above 1248 °C. Therefore, the fine two-phase microstructures observed in the Co–Cr–Si alloys are interpreted to originate from the stable β-Co_2Si phase existing at elevated temperatures. Their appearance at 1000 and 1200 °C indicates that Cr addition stabilizes the β-Co_2Si phase rather than the α-Co_2Si phase. Based on the observed microstructural changes, the phase boundaries between the α- and β-Co_2Si phases were determined. However, further investigation is required to clarify the mechanism underlying microstructure formation and the exact phase boundary between the α- and β-Co_2Si phases.

The phase equilibria of the binary silicide compounds in the Co–Cr–Si ternary system were comprehensively established. Figure 7 shows typical microstructures of the Co–Cr–Si alloys containing binary silicides after equilibration at 1000 and 1200 °C. Most of the Co–Cr–Si alloys show a coarse microstructure exceeding 5 μm for each phase. For alloys exhibiting finer microstructures, such as those shown in Fig. 7(b), quantitative analysis using FE-EPMA/WDS was conducted only in regions larger than 2 μm. In the Co–21Cr–27Si alloy heat-treated at 1200 °C for 168 h (Fig. 7(c)), the Co_3Si phase exhibits a fine microstructure that decomposes into a eutectoid microstructure of the ε(Co) and α-Co_2Si phases during water quenching. The isothermal sections of the Co–Cr–Si ternary system determined in the present work are illustrated in Fig. 8. The single-phase regions of (Co,Cr)Si, α-Co_2Si, β-Co_2Si, Cr_5Si_3, and Co_3Si extend horizontally, indicating that Cr occupies the Co site of these phases. CoSi and CrSi form a continuous solid-solution phase, designated as (Co,Cr)Si, and the solubility range of Si narrows toward the CrSi side, which are consistent with the phase diagrams proposed by Borusevich and Gladyshevskiy [14] and Kunitsin et al. [16]. The FE-EPMA/WDS measurements reveal a considerable substitution of Cr for Co in the β-Co_2Si phase, with maximum solubilities of 24.7 at% at 1000 °C and 29.6 at% at 1200 °C. On the other hand, the solubility of Co in the Cr_5Si_3 phase is 8.0 at% at 1000 and 12.1 at% at 1200 °C. For the disilicide phase in the Co–Cr–Si ternary system, the solubility of Co in $CrSi_2$ is negligible, whereas the $CoSi_2$ phase displays a solubility range extending toward the Cr-rich side. The Co_3Si phase exhibits a certain solubility range of Si on the Cr-rich side in the Co–Cr–Si ternary system, although it is typically considered a line compound in the Co–Si binary system. Kunitsin et al. [16] proposed the existence of a new ternary compound, labeled the T phase, at 1150 °C. However, our results suggest that this phase may correspond to Cr-containing Co_3Si.

4.3. Phase stability of the N phase

Figure 9 shows the three-phase microstructures containing the N phase in Co–Cr–Si alloys equilibrated at 1200 °C. The FE-EPMA/WDS measurements reveal that the N phase exhibits a solubility range of 30.5–38.5 at% Cr, while the Si content remains nearly constant at approximately 37.5 at%, as illustrated in Fig. 8(b).

Figure 10 shows the microstructures and powder XRD profiles of the Co–34.0Cr–37.5Si alloy, whose composition lies close to the single-phase region of the N phase at 1200 °C. Heat treatments were conducted at 1200 °C for 240 h (Fig. 10(a,c)) and at 1000 °C for 360 h after homogenization at 1200 °C for 240 h (Fig. 10(b,d)). As shown in Figs. 10 (a) and 10(c), microstructural observations confirm that the alloy

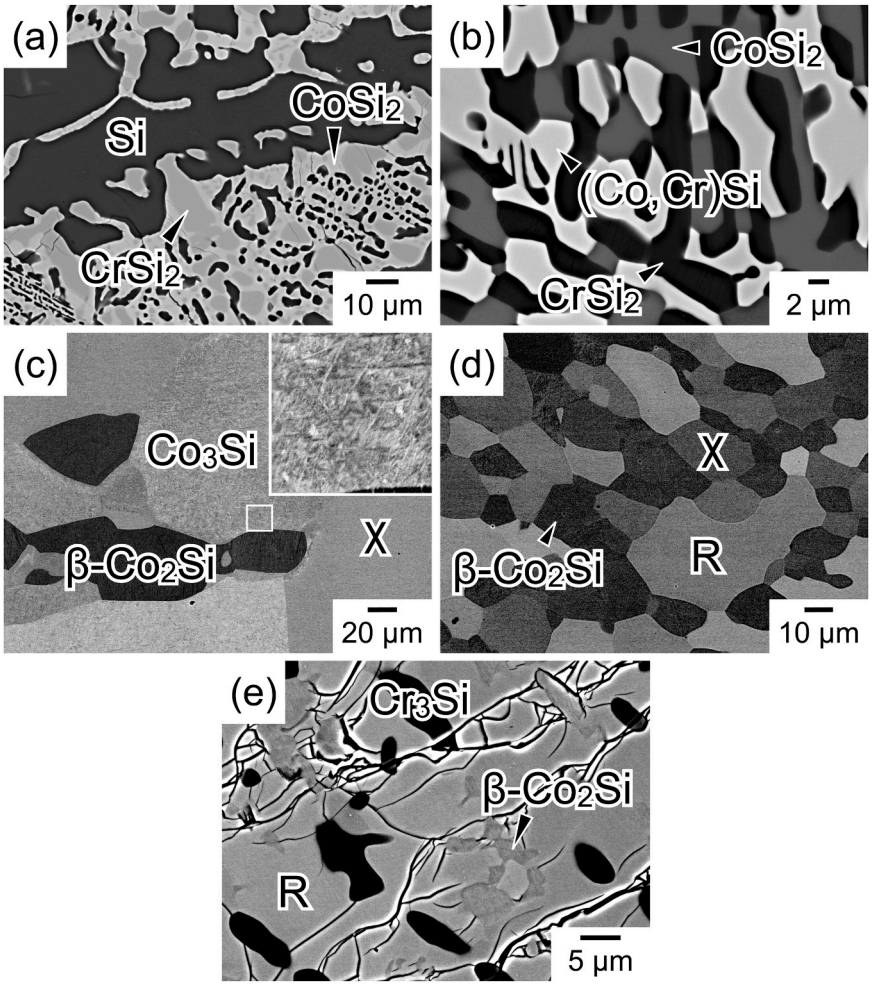


Fig. 7. BSE images of three-phase microstructures in (a) Co–10Cr–80Si alloy heat-treated at 1000 °C for 120 h, (b) Co–15Cr–60Si alloy heat-treated at 1000 °C for 168 h, (c) Co–21Cr–27Si alloy heat-treated at 1200 °C for 168 h (the inset shows the magnified view of the Co_3Si phase), (d) Co–31Cr–27Si alloy heat-treated at 1200 °C for 168 h, and (e) Co–42Cr–28Si alloy heat-treated at 1200 °C for 168 h.

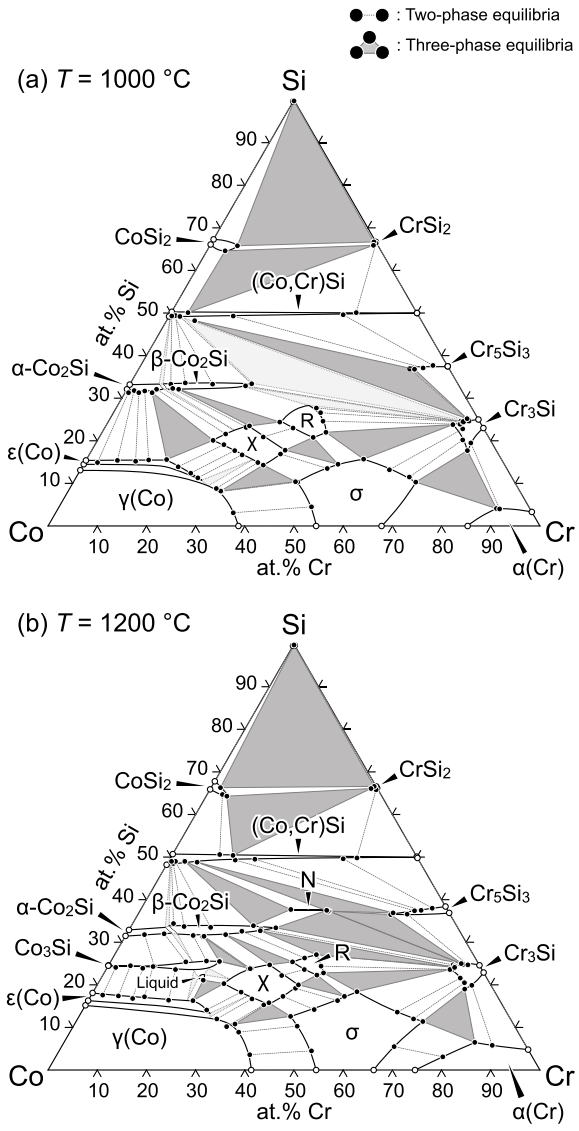


Fig. 8. Phase diagram of the Co–Cr–Si ternary system at (a) 1000 °C and (b) 1200 °C.

consists entirely of the N single phase after heat treatment at 1200 °C. Powder XRD results reveal that the N phase adopts the Mn_5Si_3-type (hP16, $P6_3/mcm$, 193) crystal structure, with lattice parameters of $a = 6.7878 \pm 0.0009$ Å and $c = 4.7400 \pm 0.0007$ Å. The XRD profile of the specimen heat-treated at 1000 °C displays peaks corresponding to the (Co,Cr)Si and Cr_3Si phases, in addition to those of the N phase (Fig. 10(b)). As shown in Fig. 10(d), this specimen exhibits a eutectoid microstructure with grey and black contrasts, as well as a phase with a white contrast. The grey phase exhibits a composition of 8.8 at% Cr and 46.7 at% Si, whereas the black phase contains 72.9 at% Cr and 24.5 at% Si. These results confirm that the eutectoid microstructure consists of the (Co,Cr)Si and Cr_3Si phases, supporting the XRD results for the specimen heat-treated at 1000 °C (Fig. 10(b)). The white phase exhibits a composition of 24.9 at% Cr and 33.1 at% Si, corresponding to the β-Co_2Si phase. These findings indicate that the N phase, which is stable at 1200 °C, decomposes at 1000 °C into β-Co_2Si and the eutectoid microstructure consisting of the (Co,Cr)Si and Cr_3Si phases. However, this decomposition appears to be sluggish, because both the XRD and FE-EPMA/WDS analyses confirm that the N phase is retained even after 360 h of heat treatment at 1000 °C (Fig. 10(b,d)). The phase equilibria established at 1000 °C (Fig. 8(a)) support the absence of the N phase at 1000 °C: In the Co–45Cr–37Si alloy annealed at 1000 °C for 1008 h, a three-phase equilibrium of the (Co,Cr)Si, Cr_5Si_3, and Cr_3Si phases is obtained. In contrast, the three-phase equilibrium involving (Co,Cr)Si, β-Co_2Si, and Cr_3Si could not be precisely determined because the microstructure was too fine to obtain accurate equilibrium compositions via FE-EPMA/WDS, even after long-term annealing.

Although Borusevich and Gladyshevskiy [14] suggested that the N phase is stable above 800 °C, they likely observed the retention of the metastable N phase owing to insufficient annealing time. According to the results of the present work, the N phase is a ternary compound stable only at high temperatures in the Co–Cr–Si system, and it is absent below 1000 °C. However, further investigation would be required to reveal the phase transformation mechanisms related to the N phase.

5. Conclusion

The phase equilibria of the Co–Cr–Si ternary system at 1000 and 1200 °C were experimentally investigated, and the following results were obtained.

(1) EBSD analysis reveals characteristic microstructural changes associated with the transition between the ε(Co) and γ(Co) phases, indicating that the ε(Co) phase disappears near compositions containing approximately 25 at% Cr and 10 at% Si.

(2) The σ-CoCr phase exhibits a wide solubility range as Si content increases, and it can contain up to 15.7 at% Si at 1000 °C and up to 18.4 at% Si at 1200 °C.

(3) Microstructural observations of the α- and β-Co_2Si phases indicate that the β-Co_2Si phase is stabilized by Cr addition in the ternary system. FE-EPMA/WDS measurements show significant substitution of Cr for Co, with maximum solubilities of 24.7 at% at 1000 °C and 29.6 at % at 1200 °C.

(4) The (Co,Cr)Si phase forms a continuous solid solution between CoSi and CrSi, with a limited Si solubility range, confirming the previously reported phase diagrams. The solubility of Co in $CrSi_2$ is negligible, whereas $CoSi_2$ exhibits a certain solubility range extending toward the Cr-rich side.

(5) The ternary χ and R compounds exhibit clear solubility ranges, as indicated in the previous work. At 1200 °C, the χ phase expands toward the Cr–Si-rich region, whereas the R phase tends to contract compared with that at 1000 °C.

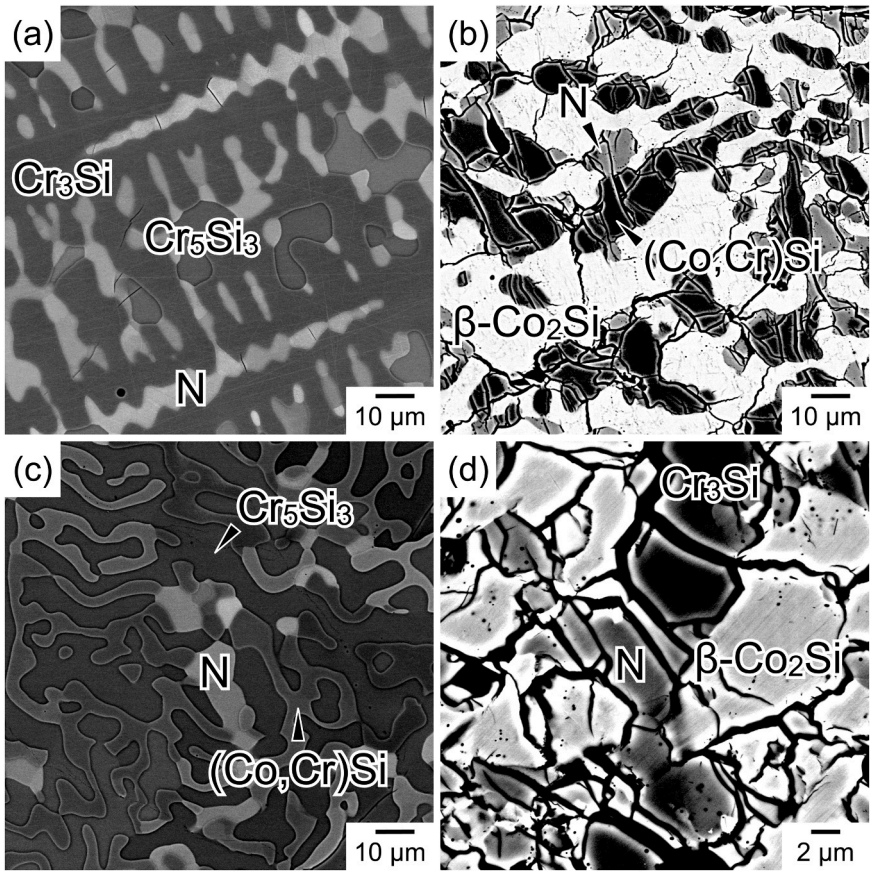


Fig. 9. BSE images of three-phase microstructures containing the N phase: (a) Co–60Cr–30Si alloy heat-treated at 1200 °C for 168 h, (b) Co–18Cr–40Si alloy heat-treated at 1200 °C for 96 h, (c) Co–32Cr–42Si alloy heat-treated at 1200 °C for 168 h, and (d) Co–41Cr–33Si alloy heat-treated at 1200 °C for 168 h.

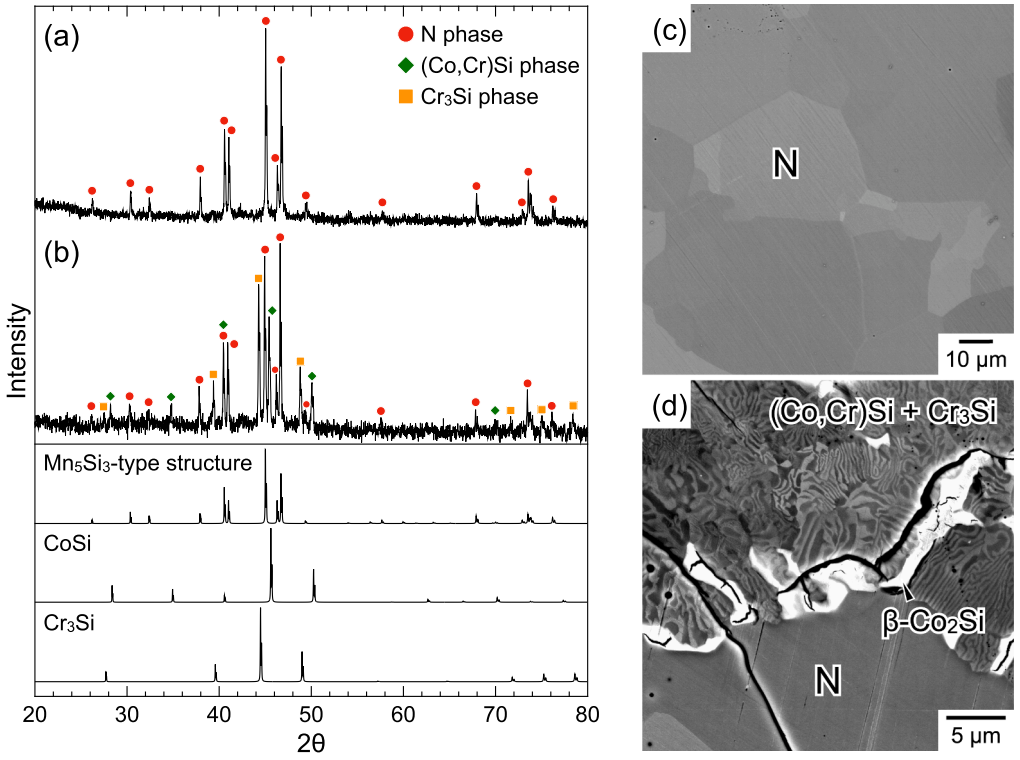


Fig. 10. Microstructures and powder XRD profiles of the Co–34.0Cr–37.5Si alloy corresponding to (a, c) equilibrated N phase after heat treatment at 1200 °C for 10 d and (b, d) non-equilibrium phase structure after heat treatment at 1200 °C for 10 d followed by 1000 °C for 15 d.

(6) The N phase is a ternary compound adopting the Mn_5Si_3-type (hP16, $P6_3/mcm$, 193) structure, and it exists as a stable phase at 1200 °C. At 1000 °C, this phase decomposes into the β-Co_2Si phase and eutectoid (Co,Cr)Si + Cr_3Si phases.

Overall, this work provides essential experimental data for the thermodynamic assessment and CALPHAD modeling of Co-based multicomponent alloys, contributing to their use in advanced biomaterials.

CRediT authorship contribution statement

Kazushige Ioroi: Writing – original draft, Visualization, Investigation, Funding acquisition. **Xiao Xu:** Writing – review & editing. **Shunya Mochimaru:** Investigation. **Toshihiro Omori:** Writing – review & editing, Supervision, Funding acquisition. **Ryosuke Kainuma:** Writing – review & editing, Supervision.

Declaration of Competing Interest

The authors declare that they have no known competing financial interests or personal relationships that could have appeared to influence the work reported in this paper.

Acknowledgements

This study was supported by JSPS KAKENHI, Japan (Grant Numbers JP21K18179 and JP25K17813).

References

[1] Q. Chen, G.A. Thouas, Metallic implant biomaterials, Mater. Sci. Eng. R Rep. 87 (2015) 1–57, https://doi.org/10.1016/j.mser.2014.10.001.
[2] M. Niinomi, M. Nakai, J. Hieda, Development of new metallic alloys for biomedical applications, Acta Biomater. 8 (2012) 3888–3903, https://doi.org/10.1016/j.actbio.2012.06.037.
[3] T. Odaira, S. Xu, K. Hirata, X. Xu, T. Omori, K. Ueki, K. Ueda, T. Narushima, M. Nagasako, S. Harjo, T. Kawasaki, L. Bodnárová, P. Sedlák, H. Seiner, R. Kainuma, Flexible and tough superelastic Co–Cr alloys for biomedical applications, Adv. Mater. 34 (2022) 2202305, https://doi.org/10.1002/adma.202202305.
[4] M. Long, H.J. Rack, Titanium alloys in total joint replacement — a materials science perspective, Biomaterials 19 (1998) 1621–1639, https://doi.org/10.1016/S0142-9612(97)00146-4.
[5] K. Ishikawa, M. Ise, I. Ohnuma, R. Kainuma, K. Ishida, Phase equilibria and stability of the bcc aluminide in the Co-Cr-Al system, Ber. Bunsenges. Phys. Chem. 102 (1998) 1206–1210, https://doi.org/10.1002/bbpc.19981020924.
[6] K. Hirata, X. Xu, T. Omori, R. Kainuma, Phase stability and magnetic properties in Co_2Cr(Al,Si) shape memory alloys, J. Magn. Magn. Mater. 500 (2020) 166311, https://doi.org/10.1016/j.jmmm.2019.166311.
[7] T. Odaira, X. Xu, A. Miyake, T. Omori, M. Tokunaga, R. Kainuma, Thermal, magnetic field- and stress-induced transformation in Heusler-type Co-Cr-Al-Si shape memory alloys, Scr. Mater. 153 (2018) 35–39, https://doi.org/10.1016/j.scriptamat.2018.04.033.
[8] K. Hirata, X. Xu, T. Omori, M. Nagasako, R. Kainuma, Martensitic transformation and superelasticity in off-stoichiometric Co_2Cr(AlSi) Heusler alloys, J. Alloy. Compd. 642 (2015) 200–203, https://doi.org/10.1016/j.jallcom.2015.03.264.
[9] K. Ioroi, X. Xu, R. Kainuma, T. Omori, Experimental determination of phase diagram and thermodynamic assessment in the Cr–Ta binary system, J. Alloy. Compd. 1018 (2025) 179195, https://doi.org/10.1016/j.jallcom.2025.179195.
[10] K. Ioroi, Y. Aono, X. Xu, T. Omori, R. Kainuma, Melting point of pure Cr and phase equilibria in the Cr–Si binary system, J. Phase Equilib. Diffus. 43 (2022) 229–242, https://doi.org/10.1007/s11669-022-00954-9.
[11] K. Ioroi, S. Mochimaru, X. Xu, R. Kainuma, T. Omori, Experimental determination of phase equilibria in the Co–Si binary system, J. Alloy. Compd. 1065 (2026) 187919, https://doi.org/10.1016/j.jallcom.2026.187919.
[12] K. Ioroi, H. Kumeta, X. Xu, R. Kainuma, T. Omori, Phase equilibria and thermodynamic assessment in the Co–Cr binary system, Calphad 90 (2025) 102853, https://doi.org/10.1016/j.calphad.2025.102853.
[13] K. Ioroi, I. Ohnuma, X. Xu, R. Kainuma, T. Omori, Thermodynamic assessment of the Cr–Si binary system, Calphad 85 (2024) 102690, https://doi.org/10.1016/j.calphad.2024.102690.
[14] L.K. Borusevich, E. Gladyshevskiy, The ternary Cr-Co-Si system, Russ. Metall. 6 (1965) 83–87.
[15] K.P. Gupta, N.S. Rajan, P.A. Beck, Effect of Si and Al on the stability of certain sigma phases, Trans. Met. Soc. AIME 218 (1960) 617–624.
[16] I.V. Kunitsin, K.B. Kalmikov, C.F. Dunaev, Isothermal section of Si-Co-Cr ternary system at 1423 K, Vestn. Mosk. Univ. Sev. 2 Khimya 37 (1996) 185–189.
[17] K.P. Gupta, The Co-Cr-Si (cobalt-chromium-silicon) system, J. Phase Equilib. Diffus. 31 (2010) 300–307, https://doi.org/10.1007/s11669-010-9670-3.
[18] T. Nishizawa, K. Ishida, The Co (cobalt) system, Bull. Alloy. Phase Diagr. 4 (1983) 387–390, https://doi.org/10.1007/BF02868089.
[19] S. Geller, V.M. Wolontis, The crystal structure of Co_2Si, Acta Cryst. 8 (1955) 83–87, https://doi.org/10.1107/S0365110X55000352.
[20] A.A. Frolov, Y.V. Putintsev, F.A. Sidorenko, P.V. Geld, R.P. Krentsis, Special features of the crystallization of Ni_2Si and Co_2Si and some characteristics of these compounds, Izv. Akad. Nauk. SSSR Neorg. Mater. 8 (1972) 468–471.
[21] Y. Wang, J. Gao, M. Kolbe, Y. Ren, D. Matson, Metastable solidification of hypereutectic Co_2Si-CoSi composition: Microstructural studies and in-situ observations, Acta Mater. 142 (2018) 172–180, https://doi.org/10.1016/j.actamat.2017.09.037.
[22] F. Wald, S.J. Michalik, The ternary system cobalt-germanium-silicon, J. Less-Common. Met. 3 (1971) 277–289, https://doi.org/10.1016/0022-5088(71)90108-1.
[23] F. Weitzer, J.C. Schuster, Phase diagrams of the ternary systems Mn, Fe, Co, Ni–Si–N, J. Solid. State Chem. 70 (1987) 178–184, https://doi.org/10.1016/0022-4596(87)90054-5.
[24] W.M. Yim, R.J. Paff, Thermal expansion of AlN, sapphire, and silicon, J. Appl. Phys. 45 (1974) 1456–1457, https://doi.org/10.1063/1.1663432.
[25] R.G. Ross, W. Hume-Rothery, High temperature X-ray metallography: I. A new Debye-Scherrer camera for use at very high temperatures II. A new parafocusing camera III. Applications to the study of chromium, hafnium, molybdenum, rhodium, ruthenium and tungsten, J. Less-Common. Met. 5 (1963) 258–270.
[26] M. Jurisch, G. Behr, Growth and perfection of chromium-silicon (Cr_3Si) single crystals, Acta Phys. Acad. Sci. Hung. 47 (1979) 201–207.
[27] R. Kieffer, F. Benesovsky, H. Schroth, The system chromium-silicon and solid solutions of silicides, Z. Met. 44 (1953) 437–442.
[28] C.H. Dauben, D.H. Templeton, C.E. Myers, The crystal structure of Cr_5Si_3, J. Phys. Chem. 60 (1956) 443–445.
[29] B. Boren, X-ray study on alloys of silicon with chromium, manganese, cobalt and nickel, *Arkiv. Kemi*, Mineral. Geol. A 11 (1933) 2–10.
[30] T. Dasgupta, J. Etourneau, B. Chevalier, S.F. Matar, A.M. Umarji, Structural, thermal, and electrical properties of $CrSi_2$, J. Appl. Phys. 103 (2008) 113516.
[31] E.I. Gladyshevskii, P.I. Kripyakevich, Y.B. Kuz'ma, Crystal structure of low-silicon ternary compounds in the Cr–Ni–Si and Cr–Co–Si systems, J. Struct. Chem. 3 (1962) 402–410, https://doi.org/10.1007/BF00744082.
[32] T. Omori, W. Ito, K. Ando, K. Oikawa, R. Kainuma, K. Ishida, FCC/HCP martensitic transformation and high-temperature shape memory properties in Co-Si alloys, Mater. Trans. 47 (2006) 2377–2380, https://doi.org/10.2320/matertrans.47.2377.